universe

MDPI

Article

Resolving Individual Massive Stars in an M31 Star Cluster Exhibiting Wolf–Rayet Features

Yunning Zhao [1,2], Yulong Gao [3,4], Wei Zhang [1,*], Fuzhen Cheng [5], Ming Yang [1], Shiming Wen [1], Shichao Han [1] and Hong Wu [1]

[1] National Astronomical Observatories, Chinese Academy of Sciences, Beijing 100101, China
[2] School of Astronomy and Space Science, University of Chinese Academy of Sciences, Beijing 100049, China
[3] Research Center of Astronomy, Qinghai University, Xining 810016, China;
[4] Department of Physics and Astronomy, Qinghai University, Xining 810016, China
[5] Department of Astronomy, University of Science and Technology of China, Hefei 230026, China;
* Correspondence: xtwfn@bao.ac.cn

Abstract

The observed ratio of Wolf–Rayet (WR) star subtypes (e.g., WC/WN) in M31 is significantly higher than the predictions of standard stellar evolution models, yet this key diagnostic discrepancy remains unresolved. This is partly due to incomplete census and the challenge of resolving individual stars in compact clusters with ground-based telescopes. In this work, we report a young cluster with WR features with the (R.A., Dec) = (00:43:39.36, +41:10:08.7), discovered with LAMOST spectra. We use the high spatial resolution of the HST imaging data to resolve the cluster members, leading to the identification of four WR star candidates, four OB stars, and one yellow supergiant. Based on the current known WR sample in M31 observed in the HST F275W filter, about one-third of WRs are contaminated by other sources within a $1\farcs1 \times 1\farcs1$ aperture, while this fraction can reach up to two-thirds for the LAMOST fiber size of $3\farcs3$. Applying the approach demonstrated in this work to a larger sample of crowded regions in M31 will yield a more complete census and allow for the measurement of a definitive WC/WN ratio, corrected for contamination. Whether this refined ratio increases or decreases the current tension with models remains to be seen, but it will provide the essential observational constraint needed to advance our understanding.

Keywords: stars: Wolf–Rayet; (stars:) supergiants; (galaxies:) Local Group

1. Introduction

Wolf–Rayet (WR) stars are the evolved descendants of massive O-type stars characterized by powerful stellar winds (1000–3000 km s^{-1}) that produce distinctive broad emission line spectra. The minimum initial mass required for a star to enter the WR phase is not a fixed value, but it depends on the adopted stellar-evolution model and physical prescriptions, including mass loss, rotation, internal mixing, binarity, and metallicity. For example, in rotating Geneva models at solar metallicity, rotation can lower the WR formation threshold from about 37 $M_\odot$ to about 22 $M_\odot$ [1], while enhanced red-supergiant mass loss can allow stars with initial masses around 20 $M_\odot$ to evolve toward WR-like stripped-envelope phases in some models [2,3]. Different theoretical frameworks, such as the Geneva models [1,4], MESA [5], PARSEC [6], and BPASS binary population models [7,8] predict different WR formation channels and lifetimes. These stars are classified into three main subtypes based on their chemical signatures: WN stars (nitrogen- and helium-dominated, products of CNO-cycle hydrogen burning), WC stars (carbon and

Check for updates

Academic Editor: Paolo Salucci

Received: 16 June 2026
Revised: 21 July 2026
Accepted: 23 July 2026
Published: 31 July 2026

Copyright: © 2026 by the authors. Licensee MDPI, Basel, Switzerland. This article is an open access article distributed under the terms and conditions of the Creative Commons Attribution (CC BY) license.

oxygen rich, from triple-α helium burning), and the rare WO subclass [9]. Transition-type WN/C stars exhibiting mixed chemistry represent a brief evolutionary phase between WN and WC stages [$\sim$1 Myr] [10,11]. Recently, Sander et al. [12] proposed that WN stars can evolve directly into the WC stage, identifying the WN/C star as their transitional type. With extreme mass-loss rates ($\sim 10^{-5}$–$10^{-4}\,M_{\odot}\,yr^{-1}$) and their eventual fate as core-collapse supernovae or gamma-ray burst progenitors, WR stars serve as crucial laboratories for studying stellar evolution, galactic chemical enrichment, and feedback mechanisms in star-forming regions [13].

WR features have been detected in extragalactic systems, where they appear as characteristic spectral "bumps" due to unresolved emission lines [14]. The "blue bump" arises from blended broad stellar lines including He II λ4686, C III/IV λ4650, and the N III λ4634–λ4641 blend, while the "red bump" corresponds to C IV λ5808-12. Ground-based telescopes cannot resolve individual WR stars in these distant systems, causing their emission features to appear blended in integrated spectra. Such systems are classified as "WR galaxies" [15]. Their WR populations make them ideal laboratories for studying recent star formation, given WR stars' short lifetimes. Initial studies using SDSS spectra found WR features in only $\sim$0.05% of galaxies (e.g., Zhang et al. [16], Brinchmann et al. [17], Agienko et al. [18]), but this low detection rate reflects SDSS's limitation to central regions or individual HII regions. The advent of IFU spectroscopy has dramatically improved detection statistics. Liang et al. [19] analyzed MaNGA's spatially resolved data for 4621 nearby galaxies, finding WR features in $\sim$2% of cases—40 times more frequently than SDSS. These datasets also enable investigations of the IMF-metallicity relation, with evidence suggesting steeper (bottom-heavy) IMFs in higher-metallicity galaxies [16,20].

As one of the nearest star-forming galaxies in the Local Group, M31 has been the subject of extensive studies of its WR population since the pioneering narrow-band imaging surveys of the 1980s [21,22]. The identification of 107 new WR stars, predominantly of the WN type, increased the total number of spectroscopically confirmed WRs in M31 to 154 [23], a sample that was further augmented by the first discovery of a WN/C transition star in this galaxy [24]. Recent discoveries of 19 additional, primarily reddened but otherwise typical WR stars in limited M31 fields imply that $\sim$60 more may remain undetected, challenging assumptions about the completeness of the current inventory [25].

Counting WR stars is essential for testing stellar evolutionary models. The commonly discussed WR-to-red supergiant (RSG) ratio (e.g., Massey et al. [26]) and the WC/WN ratio within WR populations (e.g., Neugent et al. [23]) both offer a valuable test for stellar evolutionary models. The theoretical predictions of these ratios show a strong dependence on metallicity. Because metal lines provide an important source of opacity for radiatively driven winds and WR wind mass-loss rates would depend on metallicity, especially on Fe abundance [27]. At higher metallicity, stronger winds can remove the H-rich and He-rich outer layers more efficiently, affecting both the formation of WR stars and the relative lifetimes of WN and WC phases [28]. As a result, WC stars are expected to be more common relative to WN stars in metal-rich environments, while low-metallicity galaxies should have lower WC/WN ratios [29]. However, for the WC/WN ratio, a persistent discrepancy remains between observed ratios and the predictions of single-star evolutionary models (e.g., the Geneva models [1,4], MESA models [5], PARSEC models [6], KEPLER models [30] and FRANEC models [31]), particularly at high metallicity [1,32]. This disagreement is most pronounced in M31, the highest-metallicity environment in the Local Group, where the observed ratio is dramatically larger than predicted [29]. While the use of enlarged WR samples yields a somewhat lower observed WC/WN ratio, it remains significantly higher than the predictions from single-star models at high metallicities [23,25]. Models that incorporate binary evolution, such as the Binary Population and Spectral Synthesis

(BPASS) models, provide a better match to the observations [7,8]. Yet even these models do not fully resolve the discrepancy, as their predictions at high metallicity remain lower than the observed values. Furthermore, the BPASS models do not include the effects of stellar rotation—a factor known to reduce the predicted WC/WN ratio. Accounting for rotation would therefore worsen the existing model-observation discrepancy [29].

Beyond model limitations, observational biases also affect the detection of the WR population in M31 when relying on ground-based telescopes. First, M31's substantial distance (∼780 kpc) makes its WR stars observationally fainter than those in the Milky Way. This challenge is exacerbated by a known detection bias that favors WC stars over WN stars. Because the strongest emission line in WCs is nearly four times stronger than that in WNs, making WN stars more difficult to detect at comparable brightness levels [33]. Second, the crowded environments of dense OB associations complicate the identification of even bright, strongly lined WR stars. In M33, for example, about 80% of WR stars were found within OB associations, with only 2% being truly isolated [32]. The typical half-light radius of a young cluster is 2–3 pc [34,35], which corresponds to around 2.″5 at the distance of M31. Ground-based seeing conditions of M31 (0.″9 or worse) [25] make it particularly difficult to resolve closely spaced systems where WR stars may have stellar companions or reside in crowded star-forming regions. Consequently, the current WR population statistics in M31—including both the total number of identified WR stars and the derived WC/WN ratio—are likely affected by these detection and resolution limits.

In this paper, we analyze a region exhibiting clear WR features—both blue and red bumps—in the integrated spectra, observed by the Large Sky Area Multi-Object Fiber Spectroscopic Telescope (LAMOST), combined with photometric data from the Hubble Space Telescope (HST) archive. Our goal is to resolve individual WR stars within the region covered by the fiber of the spectral observation. This method can then be extended to other regions with confirmed WR identifications and available HST observations, enabling a reassessment of the number of WR stars and the WC/WN ratio in M31.

The paper is structured as follows. In Section 2, we describe the observation of the spectrum and the imaging. Data reduction, including the photometry of the cluster, spectral flux calibration, reddening correction, and the photometry of the star members in the cluster, is presented in Section 3. The classification of the massive stars is listed in Section 4. We give the results and discussion in the last section.

2. Observation

2.1. Integrated Spectrum of the Cluster

LAMOST is a powerful tool for discovering rare objects, thanks to its large field of view (5° in diameter) and ability to obtain 4000 spectra in a single exposure [36–40]. After systematically searching spectra in the M31 region, we find a new WR feature spectrum, with the equatorial coordinates of (R.A., Dec) = (00:43:39.36, +41:10:08.7), which has been classified as a red supergiant candidate using the strength of the Ca II triplet [41], and has also been classified as a globular cluster [42].

The spectrum, obtained on 20 November 2011 with an exposure time of 1800s × 2, is shown in Figure 1. The data were reduced using the standard pipeline, which included bias subtraction, flat-field correction, spectral extraction, wavelength calibration, and flux calibration [40]. This low-resolution spectrum (R ∼ 1800) exhibits prominent blue and red bumps centered at approximately 4650 Å and 5808 Å, respectively. Due to the limited spectral resolution of LAMOST data, we cannot resolve individual components of these blended features. In addition to the broad stellar emission lines, the spectrum shows nebular emission lines ([O II], [O III], Hα, Hβ, [N II] and [S II]) and stellar absorption lines,

indicating the presence of ionized gas and other stellar sources with absorption features alongside the WR stars.

This cluster is located on the disk of M31, see the red cross in the left panel of Figure 2, with the image from Digitized Sky Survey 2 (DSS2) with a size of $3^\circ \times 3^\circ$. We zoom in this region to a size of $1.''2 \times 1.''2$ in the right panel of Figure 2, and overplot the position of the LAMOST fiber with a size of $3.''3$ in diameter in a green circle. From this figure, we cannot resolve the members in the fiber and cannot identify which member contributes to the WR feature shown in the LAMOST spectrum.

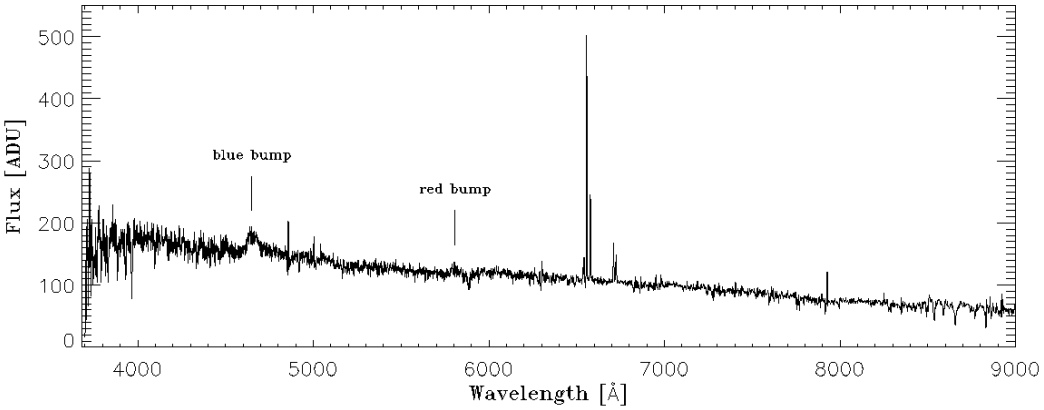

Figure 1. Optical spectrum of the target from LAMOST, showing the flux in units of ADU. The spectrum is characterized by broad WR bumps (blue and red), absorption from an underlying stellar population, and narrow nebular emission lines.

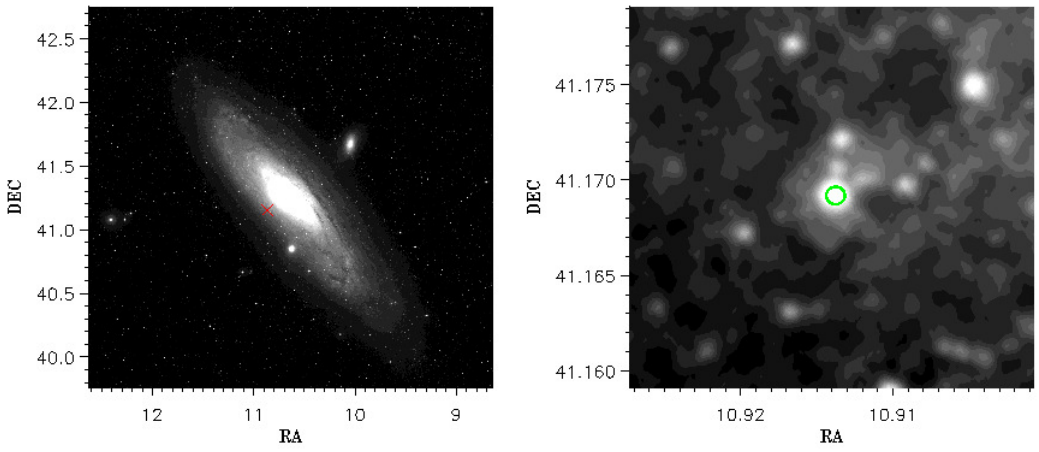

Figure 2. DSS2 image of M31. The left panel has an FOV of $2^\circ \times 2^\circ$, with the target cluster marked by a red cross. The right panel is a zoomed-in view with an FOV of $1.''2 \times 1.''2$, and the target is indicated by a green circle with a diameter of $3.''3$.

2.2. Hst Photometry Observation

The Panchromatic Hubble Andromeda Treasury (PHAT) surveys obtained imaging of M31, using HST's Wide Field Camera 3 and Advanced Camera for Surveys across six broadband filters: near-ultraviolet (F275W, F336W), optical (F475W and F814W), and near-infrared (F110W, F160W) [43]. PHAT provides precise astrometry ($<0.''1$ positional accuracy) and photometry (errors < 0.03 mag for bright sources). The imaging data were retrieved from the website of The Hubble Legacy Archive (HLA) (https://hla.stsci.edu/, accessed on 25 July 2026). We also obtained three archival F555W images from the same website: one from Proposal ID 10273 and two from Proposal ID 11647. This region was observed between 20 February 2005 and 30 December 2011. Observations were conducted four times

in the F275W, F336W, and F475W filters, three times in F555W, seven times in F814W, and twice in F110W and F160W.

The seven-band images are shown in Figure 3, with the green circles marking the positions of the LAMOST fibers (3.″3 in diameter). Thanks to the high spatial resolution and deep photometry of the HST imaging data, most stellar members within the LAMOST fiber can be resolved and identified.

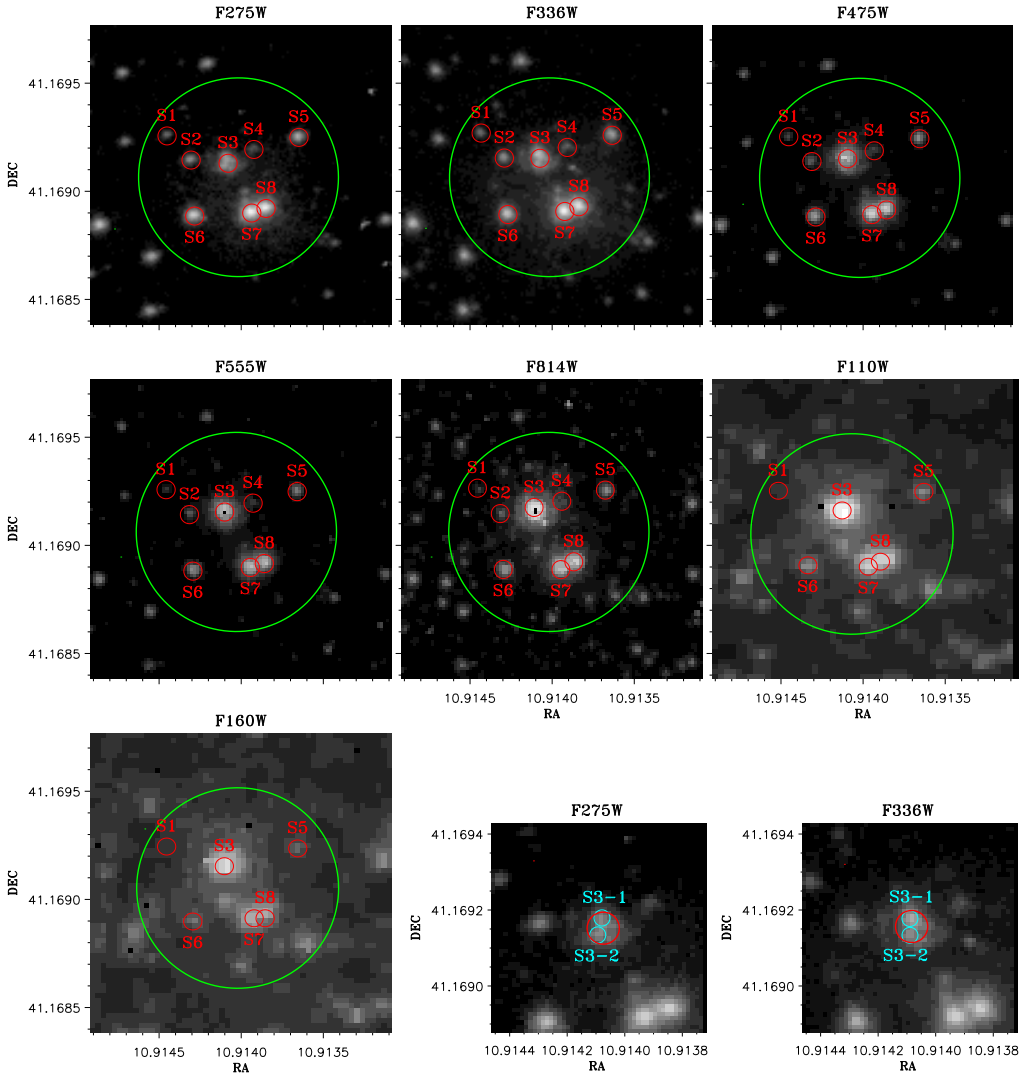

Figure 3. Multi-band images from HST observations. The first seven panels show the field in seven photometric bands, ranging from NUV to NIR. The green circle, with a diameter of 3.″3, marks the position of the LAMOST fiber. Sources S1 to S7, detected in these images, are indicated by red apertures with a radius of 0.″15. Source S3, which can be further resolved into S3-1 and S3-2 in the F275W and F336W bands, is identified in the last two panels by cyan circles with a radius of 0.″10.

3. Data Analysis

3.1. Flux Calibration

The LAMOST spectra are relatively flux-calibrated using bright stars (typically F-type stars) from the same plate. However, this method is subject to uncertainty due to the unknown foreground extinction of the calibrating star. To address this, we performed aperture photometry on HST imaging data to measure magnitudes within the LAMOST fiber aperture. The results are listed in Table 1 (see the S_{tot} values).

For the flux recalibration of the LAMOST spectrum, we selected three HST filters (F475W, F555W, and F814W) that match its wavelength coverage. The upper panel of Figure 4 shows the recalibrated spectrum, with the corresponding HST photometric measurements marked as cyan stars.

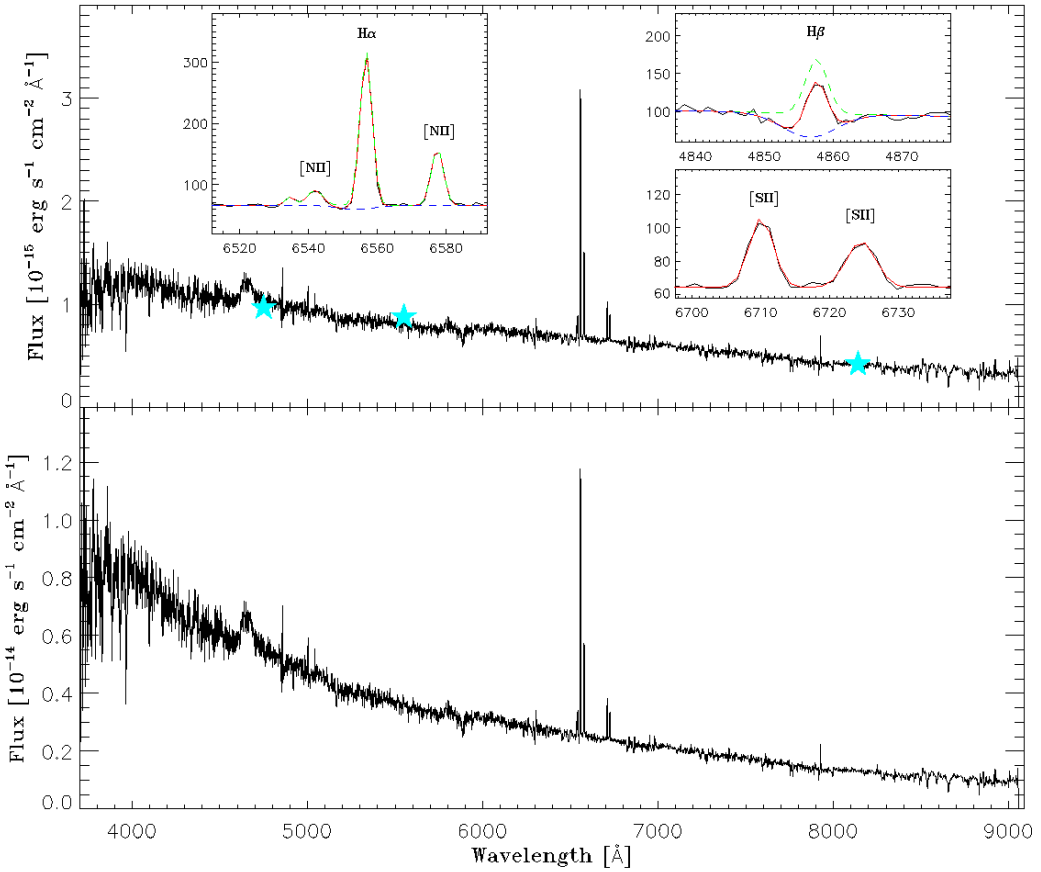

Figure 4. (**Upper**) Re-calibrated spectrum shown in black line over-plotted with the calibrating HST photometry (F475W, F555W, and F814W bands) indicated by filled cyan stars. The inserts show multi-Gaussian fits to the [N II], Hα, Hβ, and [S II] lines, where the nebular, stellar absorption, and total components are represented by green dashed, blue dashed, and red solid lines, respectively. (**Lower**) De-reddened spectrum, derived using the Balmer decrement method.

Table 1. Photometric data—including source ID and coordinates—for S_{tot}, S1–S8, and the resolved sources S3-1 and S3-2. The data are listed separately for both the original and de-reddened values.

(1) OBJ	(2) RA	(3) DEC	(4) m(F275W)	(5) m(F336W)	(6) m(F475W)	(7) m(F555W)	(8) m(F814W)	(9) m(F110W)	(10) m(F160W)
original									
S_{tot}	00 43 39.4	41 10 08.7	17.48 ± 0.00	17.22 ± 0.01	16.74 ± 0.02	16.51 ± 0.19	16.48 ± 0.16	16.39 ± 0.01	16.68 ± 0.09
S1	00 43 39.5	41 10 09.4	23.39 ± 0.03	23.31 ± 0.10	22.92 ± 0.02	23.10 ± 0.02	23.37 ± 0.07	23.64 ± 0.40	24.07 ± 0.36
S2	00 43 39.4	41 10 08.9	22.15 ± 0.02	22.08 ± 0.02	21.90 ± 0.03	21.93 ± 0.06	22.10 ± 0.04	-	-
S3	00 43 39.4	41 10 08.9	20.52 ± 0.02	19.73 ± 0.02	18.49 ± 0.01	17.66 ± 0.47	17.73 ± 0.30	17.56 ± 0.06	18.01 ± 0.08
S3-1	00 43 39.4	41 10 09.0	21.71 ± 0.11	20.38 ± 0.02	-	-	-	-	-
S3-2	00 43 39.4	41 10 08.8	21.68 ± 0.05	21.78 ± 0.18	-	-	-	-	-
S4	00 43 39.3	41 10 09.1	23.35 ± 0.02	23.11 ± 0.06	22.68 ± 0.14	22.45 ± 0.10	22.51 ± 0.53	-	-
S5	00 43 39.3	41 10 09.3	21.29 ± 0.04	21.21 ± 0.05	20.86 ± 0.03	20.88 ± 0.01	21.15 ± 0.07	21.59 ± 0.06	22.52 ± 0.42
S6	00 43 39.4	41 10 08.0	20.13 ± 0.05	20.11 ± 0.02	20.14 ± 0.03	20.20 ± 0.11	20.49 ± 0.07	21.23 ± 0.05	22.02 ± 0.21
S7	00 43 39.3	41 10 08.1	18.69 ± 0.02	18.42 ± 0.04	18.25 ± 0.05	18.30 ± 0.12	18.50 ± 0.29	19.11 ± 0.21	19.64 ± 0.28
S8	00 43 39.3	41 10 08.1	18.97 ± 0.03	18.72 ± 0.05	18.49 ± 0.04	18.52 ± 0.06	18.67 ± 0.10	19.08 ± 0.19	19.70 ± 0.04
de-reddened									
S_{tot}	00 43 39.4	41 10 08.7	14.79 ± 0.00	14.90 ± 0.01	14.91 ± 0.02	14.83 ± 0.19	15.22 ± 0.16	15.39 ± 0.01	15.87 ± 0.09
S1	00 43 39.5	41 10 09.4	20.70 ± 0.03	20.99 ± 0.10	21.09 ± 0.02	21.42 ± 0.02	22.10 ± 0.07	22.64 ± 0.40	23.27 ± 0.36

Table 1. *Cont.*

(1) OBJ	(2) RA	(3) DEC	(4) m(F275W)	(5) m(F336W)	(6) m(F475W)	(7) m(F555W)	(8) m(F814W)	(9) m(F110W)	(10) m(F160W)
S2	00 43 39.4	41 10 08.9	19.46 ± 0.02	19.76 ± 0.02	20.06 ± 0.03	20.25 ± 0.06	20.83 ± 0.04	-	-
S3	00 43 39.4	41 10 08.9	17.83 ± 0.02	17.41 ± 0.02	16.65 ± 0.01	15.98 ± 0.47	16.46 ± 0.30	16.56 ± 0.06	17.21 ± 0.08
S3-1	00 43 39.4	41 10 09.0	19.04 ± 0.11	18.06 ± 0.02	-	-	-	-	-
S3-2	00 43 39.4	41 10 08.8	19.01 ± 0.05	19.46 ± 0.18	-	-	-	-	-
S4	00 43 39.3	41 10 09.1	20.66 ± 0.02	20.79 ± 0.06	20.85 ± 0.14	20.77 ± 0.10	21.24 ± 0.53	-	-
S5	00 43 39.3	41 10 09.3	18.60 ± 0.04	18.89 ± 0.05	19.02 ± 0.03	19.20 ± 0.01	19.88 ± 0.07	20.59 ± 0.06	21.72 ± 0.42
S6	00 43 39.4	41 10 08.0	17.44 ± 0.05	17.79 ± 0.02	18.30 ± 0.03	18.52 ± 0.11	19.22 ± 0.07	20.23 ± 0.05	21.21 ± 0.21
S7	00 43 39.3	41 10 08.1	16.00 ± 0.02	16.10 ± 0.04	16.41 ± 0.05	16.62 ± 0.12	17.23 ± 0.29	18.11 ± 0.21	18.84 ± 0.28
S8	00 43 39.3	41 10 08.1	16.28 ± 0.03	16.40 ± 0.05	16.65 ± 0.04	16.84 ± 0.06	17.40 ± 0.10	18.08 ± 0.19	18.89 ± 0.04

3.2. Line Measurement and Extinction Correction

The fitting results for Hα, Hβ, [N II] and [S II] lines are displayed in the small insets of the upper panel in Figure 4, where black lines represent the observed spectrum and red lines show the fitted profiles. For the [S II] doublet, we used two separate Gaussian components, while the Balmer lines (Hα and Hβ) required more components due to stellar absorption superposed on nebular emission. Specifically, Hβ was fitted with two Gaussians (nebular emission: cyan dashed line; stellar absorption: blue dashed line), and Hα was treated similarly but included three additional components to account for the [N II] doublet and an unidentified emission feature (centered at ∼6534.6 Å). The derived radial velocities (RVs), integrated fluxes, and FWHMs are summarized in Table 2. The emission-line radial velocities (RVs; ∼360 km/s) confirm that the emission nebulae are located in M31.

Table 2. Measurements of the radial velocity, integrated flux, and FWHM for the Hβ, [N II], Hα, and [S II] lines.

(1) Line	(2) RV (km s^{-1})	(3) Flux (erg s^{-1}cm^{-2})	(4) FWHM (Å)	(5) Flux^{d} (erg s^{-1}cm^{-2})
Hβ	−317.18 ± 1.57	285.86 ± 15.31	3.68 ± 0.09	1488.12 ± 79.68
Hβ [a]	−379.09 ± 7.19	−309.32 ± 15.04	9.19 ± 0.34	
[N II]	−367.05 ± 4.52	140.10 ± 7.98	5.23 ± 0.26	534.76 ± 30.47
Hα	−363.99 ± 0.39	1117.71 ± 9.58	4.14 ± 0.02	4257.19 ± 36.47
Hα [a]	−489.83 ± 43.38	−90.16 ± 0.00	12.55 ± 2.21	
[N II]	−360.40 ± 0.86	412.14 ± 3.98	4.18 ± 0.05	1565.16 ± 15.11
[S II]	−368.28 ± 1.86	183.42 ± 3.98	4.12 ± 0.10	683.78 ± 14.83
[S II]	−362.08 ± 3.13	147.84 ± 4.45	5.04 ± 0.17	550.04 ± 16.56

[a] Stellar absorption component. [d] De-reddended integrated flux.

The Hβ emission in the blue part of the spectrum shows a significant velocity offset compared to the Hα, [N II], and [S II] emissions in the red part. This discrepancy likely arises because the wavelength calibration was performed separately for the red and blue spectral regions. Additionally, the stellar component exhibits a blueshift in RVs relative to the nebular component. However, the RV values still support their association with M31 rather than being foreground Galactic stars.

We measure the observed Balmer decrement $(F_{H\alpha}/F_{H\beta})_{obs} = 3.91 \pm 0.21$. Using the intrinsic ratio $(F_{H\alpha}/F_{H\beta})_{int} = 2.86$ and adopting the extinction law which was introduced by Charlot and Fall [44]

$$F_\lambda = F_\lambda^{obs} \exp\left[\tau\left(\frac{\lambda}{5500}\right)^{-0.7}\right] \quad (1)$$

The optical depth τ at 5500 Å (τ_V) is derived from

$$\tau_V = -\frac{\ln(F_{H\alpha}/F_{H\beta})_{obs} - \ln(F_{H\alpha}/F_{H\beta})_{int}}{(\lambda_{H\alpha}/5500)^{-0.7} - (\lambda_{H\beta}/5500)^{-0.7}} \quad (2)$$

This yields $\tau_V = 1.51 \pm 0.27$.

The attenuation derived from this method corresponds to that of the gas, i.e., $E(B-V)_{gas} = 2.5\,\tau_V$. The stellar attenuation $E(B-V)_{star}$, however, is not always identical to it. The ratio $f = E(B-V)_{star}/E(B-V)_{gas}$ typically ranges from about 0.44 to ~1. Li et al. [45] further reported an anti-correlation between $E(B-V)_{star}$ and the luminosity-weighted stellar age t_L. Because the region studied in this work is young, the value of f should be significantly larger than 0.44. For simplicity, we assume $f = 1$ in this region and apply the corresponding extinction correction to the observed spectrum, broadband magnitudes, and emission-line fluxes. The bottom panel of Figure 4 presents the de-reddened spectrum. The de-reddened total magnitudes for each band are summarized in Table 1, while the de-reddened emission-line fluxes are listed in column 5 of Table 2.

3.3. Property of the Ionized Medium

Using the de-reddened [S II] $\lambda6717/\lambda6731$ line ratio of 1.24 ± 0.06 and adopting electron temperature T_e = 10,000 K, we applied Equation (3) of Proxauf et al. [46] to derive an electron density of $n_e = 136 \pm 56$ cm^{-3}. We also estimated the oxygen abundance using two independent methods: the N2 method [47], which yielded 12 + log(O/H) = 8.652 $\pm$ 0.003, and the N2S2Hα method [48], which gave 12 + log(O/H) = 8.76 $\pm$ 0.01. Adopting the solar oxygen abundance 12 + log(O/H) = 8.69 from Asplund et al. [49], these values indicate that this region has an approximately solar oxygen abundance.

3.4. Photometry of HST Images for Resolved Targets

Thanks to HST's superior spatial resolution, we performed photometry on resolved targets within 3.″3 regions. Using an fixes aperture radius of 0.″15 (red circles in Figure 3), we identified and measured eight targets (labeled S1–S8). Additionally, we detected numerous faint sources in F814W that were absent in shorter wavelength filters, indicating red spectral energy distributions. These objects were undetectable in longer wavelength filters (F110W and F160W) due to their lower spatial resolution. As our study focuses on massive stars, we excluded these faint, red objects from subsequent analysis. The exceptional resolution of the F275W and F336W filters allowed us to resolve S3 into two distinct components (S3-1 and S3-2, marked by cyan circles in the last two panels of Figure 3), for which we used a smaller 0.″075 aperture for precise photometry. The measured magnitudes are presented in Table 1, along with de-reddened magnitudes calculated using the extinction correction method described in Section 3.2. The uncertainties of magnitudes are derived from the scatter of multi-epoch observation in each band.

Figure 5 displays the spectral energy distributions (SEDs) for the nine objects. The left panels present observed magnitudes (open black circles), while the right panels show absolute magnitudes (open black circles) corrected for extinction and adjusted to a distance modulus of 24.46 for M31. Sources S1, S5–S8 are detected in all seven bands, whereas S2 and S4 lack detections in F110W and F160W. S3 appears in all bands (open black circles), while its resolved components S3-1 and S3-2 (red and blue open circles, respectively) are only detected in the higher-resolution F275W and F336W bands.

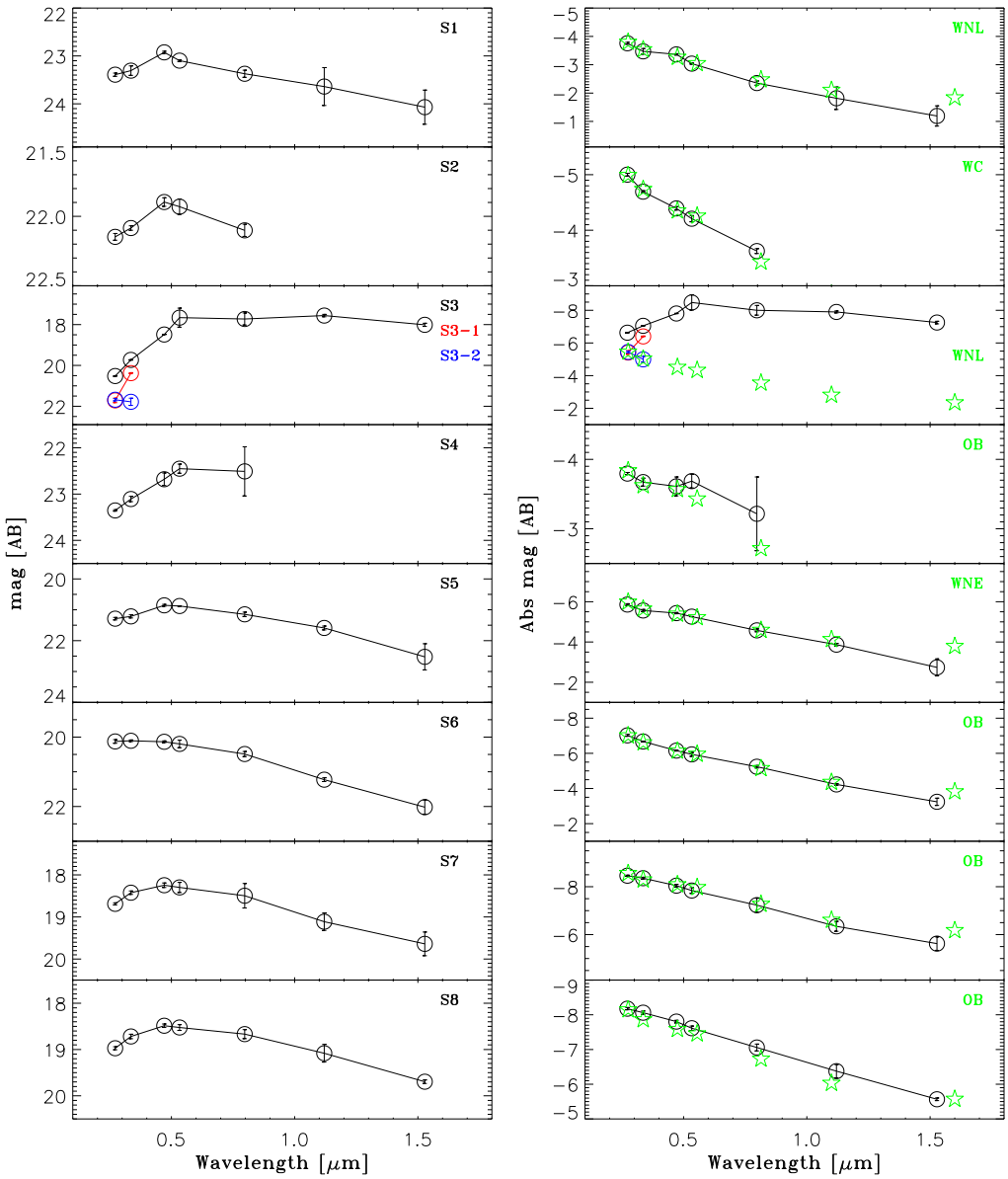

Figure 5. (**Left**) Observed SEDs (black circles with lines) for the sources, with the resolved components S3-1 and S3-2 colored red and blue. (**Right**) De-reddened SEDs in absolute magnitudes, compared with the best-fitting PoWR models (open green stars). Each panel is annotated with the source ID or classification in the upper-right corner.

4. Identifying the Spectra Types

Although we lack individual spectra for each star, by combining multi-band photometry (from FUV to NIR) with the integrated LAMOST spectrum, we can still constrain spectral types and identify potential WR stars contributing to the observed WR features (both red and blue bumps).

Except S3, the SEDs of all targets display characteristically blue slopes, consistent with early-type stellar photospheres. We determine fundamental stellar parameters by fitting these SEDs with synthetic spectra from the Potsdam Wolf–Rayet (PoWR) model atmospheres [50–52], which incorporate non-local thermal equilibrium (non-LTE) physics, spherical expansion, and metal line blanketing. For this study, we utilize the publicly available model grids with fixed Galactic metallicity from the PoWR database (http://www.astro.physik.uni-potsdam.de/PoWR.html, accessed on 25 July 2026), including: (1) WN

star models [53,54], (2) WC star models [55], and (3) OB star models [56]. This metallicity is justified by the oxygen abundance measured in Section 3.3, which is comparable to the solar value. We compare the observed SEDs to the model grids and select the model with the minimum χ^2 as the best fit. The best-fitting results are shown as green stars in the right panels of Figure 5, with the corresponding classifications indicated in the upper right corners. We also list their classifications and fitting stellar parameters in Table 3. The uncertainties of the fitted stellar parameters are estimated by propagating the photometric uncertainties, which are derived from the scatter of the multi-epoch HST measurements in each band, as described in Sections 2.2 and 3.4. The masses listed in Table 3 are current stellar masses inferred from the best-fitting PoWR atmosphere models, rather than initial or zero-age main-sequence (ZAMS) masses. We note that the derived parameters are model-dependent, because they are based on broadband SED fitting and the assumptions of the adopted PoWR atmosphere-model grids. In particular, the mass-loss rates and terminal velocities are constrained by the selected PoWR models rather than directly measured from spatially resolved stellar spectra. Our SED fitting results indicate that sources S1, S2, and S5 are WR stars candidates, while S4, S6, S7, and S8 are OB stars. It should be noted that these WR star classifications are based solely on broadband SED fitting, so we regard them as WR star candidates. Definitive certification of these WR sources require more spatially resolved spectroscopic observations in the future.

For S3, we resolve it into S3-1 and S3-2 using imaging data in previous section. S3-2 exhibits blue slope, while S3-1 shows red slope. Although the object S3-2 has only two bands of observational data, we still perform SED fitting as other early-type sources. We also present the fitting results across all seven bands, as we will subtract its contribution from the SED of S3 to isolate the SED of S3-1. For S3-2, the classification is ambiguous due to having only two UV photometric bands. To resolve this, we combine the modeled WR spectra of S1, S2, and S5 to compute the expected blue and red bump fluxes. The results indicated a significant deficit, requiring an additional WR contribution. Consequently, we classify S3-2 as a WR star candidate, with a template fit identifying it as a WNL subtype. The classification and stellar parameters of S3-2 are also listed in Table 3. Including S3-2 with the other three WR stars yields integrated blue and red bump fluxes of 1.9×10^4 erg s^{-1} cm^{-2} and 3.6×10^5 erg s^{-1} cm^{-2}, respectively, which are consistent with the values of $(4.2 \pm 0.4) \times 10^4$ erg s^{-1} cm^{-2} and $(2.6 \pm 2.5) \times 10^5$ erg s^{-1} cm^{-2} derived from the observed LAMOST spectra.

After subtracting the contribution of S3-2 from S3, the resulting SED for S3-1 exhibits a red shape. Its absolute magnitude ($M(F555W) = -8.47 \pm 0.47$) suggests a supergiant. Initial attempts to fit the entire SED with standard templates were unsuccessful, likely due to excess UV emission from an unresolved companion—a common feature in binary systems containing supergiants [57]. Therefore, we uSED the VO SED Analyzer (VOSA) [58] to fit only the longer-wavelength portion of the SED (green line in Figure 6) with ATLAS9 models [59]. A good match was obtained with a yellow supergiant template characterized by $T_{\rm eff} = 6500 \pm 125$ K, $\log g = 0.50 \pm 0.40$, and $\log(L/L_\odot) = 5.050 \pm 0.002$. As the most luminous cluster member, S3-1 dominates the red portion of the integrated light. Although its UV classification remains uncertain due to limited data, this has a negligible impact on the longer-wavelength analysis. Our analysis thus reveals that the cluster's prior classification as a red supergiant stems from the overwhelming dominance of this single supergiant's light.

We checked the yellow and red supergiant catalogs of Drout et al. [60], Gordon et al. [61], and Wu et al. [62], and found that S3-1 is not included in these catalogs. Since S3-1 is located within the same compact stellar system, we consider it likely to be physically associated with the system, although a chance projection along the line of sight cannot be completely

ruled out without spatially resolved spectroscopy or kinematic information. If S3-1 is a coeval member, its coexistence with the WR/OB candidates may be explained by different evolutionary timescales for stars with different initial masses.

As we only identify the brightest stars in the LAMOST fiber, and there are also contributions from fainter stars and ionized gas within the same fiber, we did not attempt to combine the SEDs of all individual stars for comparison with the observed LAMOST spectrum. We must acknowledge that the current SED composition may not be unique, as certain subtypes of WR and OB stars often exhibit similar SEDs due to their comparable luminosities and temperatures. We consider this the most probable composition, and we look forward to higher-spatial-resolution spectra to confirm the stars within this cluster.

Table 3. Stellar classification and physical parameters for the observed sources (S1, S2, S4–S8) and the resolved sub-component S3-2.

(1) OBJ	(2) Type	(3) T_* (kK)	(4) log R_t ($R_\odot$)	(5) log L ($L_\odot$)	(6) M_*^1 ($M_\odot$)	(7) log $\dot{M}$ ($M_\odot$ yr^{-1})	(8) v_∞ (km s^{-1})
S1	WNL	99 ± 1	0.70 ± 0.02	$5.30 \pm -$	$29.90 \pm -$	-5.49 ± 0.02	$1000 \pm -$
S2	WC	70 ± 1	0.81 ± 0.03	$5.30 \pm -$	$11.60 \pm -$	-5.09 ± 0.02	$2000 \pm -$
S3-2	WNL	$50 \pm -$	1.55 ± 0.11	$5.30 \pm -$	$29.90 \pm -$	-5.86 ± 0.17	$999 \pm -$
S4	OB	$19 \pm -$	2.26 ± 0.02	$3.96 \pm -$	$9.19 \pm -$	-7.00 ± 0.00	863 ± 91
S5	WNE	46 ± 2	0.84 ± 0.11	$5.30 \pm -$	$12.00 \pm -$	-4.48 ± 0.08	$1600 \pm -$
S6	OB	43 ± 3	2.87 ± 0.02	5.80 ± 0.10	59.54 ± 12.05	$-7.00 \pm -$	3039 ± 358
S7	OB	22 ± 2	3.18 ± 0.06	5.82 ± 0.08	46.44 ± 5.90	$-7.00 \pm -$	1212 ± 351
S8	OB	27 ± 2	3.13 ± 0.01	5.89 ± 0.10	52.57 ± 8.24	$-7.00 \pm -$	1668 ± 161

[1] Current stellar mass.

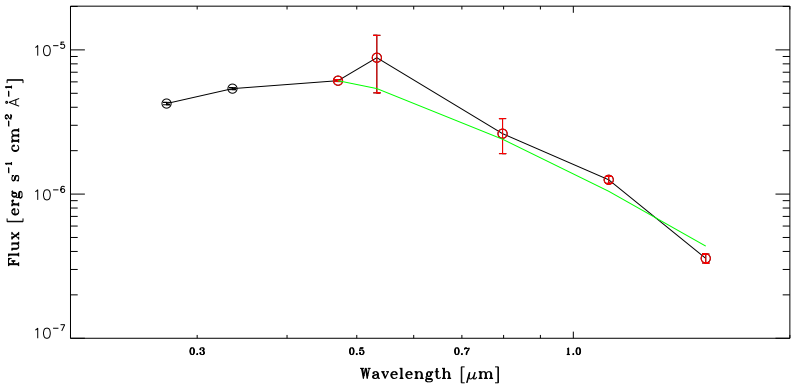

Figure 6. SED of S3-1. The observed data (open circles with black line) is fitted by a model (green line) using the data points highlighted in red.

5. Summary and Discussion

- We have discovered a cluster in M31 that exhibits WR features using LAMOST spectra. While previous ground-based observations identified this cluster as a single supergiant star based on its SED, our analysis of high spatial resolution HST multi-band data (spanning UV to IR) resolves nine individual members: four WR star candidates, four OB stars, and one yellow supergiant. The presence of these massive stars suggests that the region is young and has recently undergone a new process of star formation.
- The yellow supergiant dominates the cluster's emission at red wavelengths, explaining why earlier ground-based studies misclassified the entire cluster as a single supergiant. Furthermore, our inability to fully fit the UV emission from this supergiant suggests the presence of an unresolved companion.
- These results highlight the crucial role of high spatial resolution in properly identifying cluster members in M31. They also imply that binary fraction estimates for supergiants in M31 based on ground-based data are affected by such unresolved systems.

To better determine the WC/WN ratio in nearby galaxies like M31, M33, LMC, and SMC, and to investigate its metallicity dependence while comparing with theoretical models, it is necessary to re-examine regions showing WR features in ground-based spectra and to identify unresolved WR stars using existing HST or JWST data. These preparatory studies will establish a reliable census of WR populations for detailed analysis. In Appendix A, we use a combined WR catalog and HST images to discuss what fraction of WR stars in M31 might be contaminated when observed with a LAMOST-sized fiber.

The Habitable Worlds Observatory (HWO) will revolutionize massive star studies by enabling panchromatic, spatially resolved ($\leq 0\farcs015$) observations of individual stars across the Local Volume ($\sim$5 Mpc) [63]. With resolution surpassing HST and JWST, HWO will provide unprecedented precision in characterizing WR populations, allowing us to accurately measure WC/WN ratios across metallicities, directly test stellar evolution models, and reveal how massive star evolution varies in different galactic environments. This capability will open a new era in understanding WR stars and their role in galactic ecosystems.

Author Contributions: Conceptualization and methodology, W.Z.; software, W.Z. and Y.Z.; validation, Y.G. and M.Y.; formal analysis, Y.Z. and W.Z.; investigation, Y.Z., W.Z. and S.W.; data curation, W.Z., Y.G. and M.Y.; writing—original draft preparation, Y.Z. and W.Z.; writing—review and editing, Y.Z., W.Z., Y.G., M.Y. and S.H.; visualization, Y.Z.; supervision, F.C. and H.W.; project administration, W.Z. and H.W.; funding acquisition, W.Z. and H.W. All authors have read and agreed to the published version of the manuscript.

Funding: This work is supported by the National Key R&D Program of China grants (Nos. 2021YFA1600401 and 2021YFA1600400) and the National Natural Science Foundation of China (NSFC) (Nos. 12090041, and 12090040). This work is also sponsored by the Strategic Priority Research Program of the Chinese Academy of Sciences (No. XDB0550100).

Data Availability Statement: This work made use of the data from LAMOST (Large Sky Area Multi-Object Fiber Spectroscopic Telescope, also known as the Guoshoujing Telescope) (https://cstr.cn/31118.02.LAMOST, accessed on 25 July 2026). LAMOST is a Chinese national mega-science facility, operated by the National Astronomical Observatories, Chinese Academy of Sciences. This publication makes use of VOSA, developed under the Spanish Virtual Observatory (https://svo.cab.inta-csic.es, accessed on 25 July 2026) project funded by MCIN/AEI/10.13039/501100011033/ through grant PID2020-112949GB-I00. VOSA has been partially updated by using funding from the European Union's Horizon 2020 Research and Innovation Programme, under grant agreement No. 776403 (EXOPLANETS-A).

Acknowledgments: We thank the anonymous reviewers for their constructive comments and suggestions, which helped improve the clarity and quality of this manuscript. W.Z. thanks Cheng Li and Yang Huang for helpful suggestions.

Conflicts of Interest: The authors declare no conflicts of interest.

Appendix A

To systematically determine what fraction of WR stars in M31 might be contaminated when observed with a LAMOST-sized fiber, we used a combined WR catalog from Neugent et al. [23], Shara et al. [24], and Neugent and Massey [25], containing a total of 174 unique WR stars.

We cross-matched this sample with the HST archive data and found that 91 of these stars have been observed with the F275W filter. In this section, we only count the number of bright stars in the images, and do not perform SED fitting, as most of these WR stars are either not observed by LAMOST or do not have high signal-to-noise spectra. By visually inspecting these images in Figure A1, we found that 34 out of 91 (37.4%) appear isolated within a diameter circular aperture, meaning no other bright sources are present. The re-

maining 57 sources (62.6%) show two or more bright objects within the same aperture, implying that spectroscopic observations with LAMOST would suffer from significant contamination from nearby stars. This will potentially affect the WR stars census and the analysis of the WC/WN ratio in M31.

We repeated this analysis using a smaller $1''.1 \times 1''.1$ square aperture to simulate a higher-resolution fiber. Within this smaller region, 63 WR stars (69.2%) appear single, while 28 (30.8%) still show evidence of contamination.

The catalog of unique WR stars in M31 used in this analysis is presented in Table A1. For each source, the table provides an ID (1–174), J2000 coordinates (RA and Dec), and a flag (Y/N) denoting availability of HST F275W imaging. Columns 5 and 6 give the results of our visual contamination assessment for two aperture sizes: a LAMOST-sized fiber and a smaller $1''.1 \times 1''.1$ square aperture, with entries labeled 'single' or 'multiple'.

Table A1. Unique sample of WR stars in M31. The columns are as follows: (1) the ID number (ranging from 1 to 174); (2) and (3) the J2000 RA and Dec; (4) a flag (Y/N) indicating whether the star has been observed with the HST F275W filter; (5) a classification flag (S/M: single/multiple) based on a visual inspection for contamination within a LAMOST-sized fiber aperture; (6) the same classification as column 5, but for a $1''.1 \times 1''.1$ square aperture; and (7) the reference catalog: N12, [23]; N23, [25]; S16, [24].

(1) ID	(2) RA	(3) Dec	(4) F275W	(5) n(3″.3)	(6) n(1″.1)	(7) Ref
001	00:38:57.19	+40:31:32.2	N	-	-	N12
002	00:39:11.04	+40:38:17.5	N	-	-	N12
003	00:39:19.53	+40:22:11.6	N	-	-	N12
004	00:39:33.46	+40:20:18.9	Y	S	S	N12
005	00:39:35.63	+40:28:11.5	N	-	-	N12
006	00:39:39.61	+40:20:31.1	Y	M	S	N12
007	00:39:39.97	+40:34:50.4	N	-	-	N12
008	00:39:45.82	+40:23:03.2	N	-	-	N12
009	00:39:48.84	+40:52:56.3	N	-	-	N12
010	00:40:02.84	+40:38:52.8	N	-	-	N12
011	00:40:05.65	+40:58:48.1	N	-	-	N12
012	00:40:19.47	+40:52:24.9	N	-	-	N12
013	00:40:20.44	+40:48:07.7	N	-	-	N12
014	00:40:21.13	+40:35:20.6	N	-	-	N12
015	00:40:22.43	+40:52:34.6	N	-	-	N12
016	00:40:23.02	+40:44:54.1	Y	S	S	N12
017	00:40:24.33	+40:50:16.2	N	-	-	N12
018	00:40:26.23	+40:44:59.6	Y	M	M	N12
019	00:40:29.27	+40:39:16.6	N	-	-	N12
020	00:40:31.67	+40:39:09.0	N	-	-	N12
021	00:40:32.58	+40:35:50.1	N	-	-	N12
022	00:40:34.17	+40:43:40.4	N	-	-	N12
023	00:40:34.69	+40:44:32.9	Y	S	S	N12
024	00:40:35.18	+40:38:38.5	N	-	-	N12
025	00:40:36.76	+41:01:04.3	N	-	-	N12
026	00:40:43.28	+40:35:25.2	N	-	-	N12
027	00:40:56.49	+41:03:08.7	Y	S	S	N12
028	00:40:56.72	+41:02:55.4	Y	S	S	N12
029	00:40:58.49	+41:04:14.8	Y	S	S	N12
030	00:40:59.13	+40:36:52.0	N	-	-	N12
031	00:41:00.97	+40:36:33.0	N	-	-	N12
032	00:41:02.04	+41:04:46.0	N	-	-	N12
033	00:41:07.31	+41:04:17.0	N	-	-	N12

Table A1. *Cont.*

(1) ID	(2) RA	(3) Dec	(4) F275W	(5) n(3.″3)	(6) n(1.″1)	(7) Ref
034	00:41:09.46	+40:49:07.8	Y	M	M	N12
035	00:41:09.59	+40:48:56.2	Y	M	S	N12
036	00:41:14.95	+40:44:48.2	N	-	-	N12
037	00:41:15.95	+41:09:06.8	N	-	-	N12
038	00:41:26.11	+41:12:20.0	Y	M	S	N12
039	00:41:26.39	+41:12:03.5	Y	M	M	N12
040	00:41:29.11	+41:13:11.4	Y	M	M	N12
041	00:41:29.17	+41:13:35.0	Y	M	M	N12
042	00:41:30.37	+41:05:00.9	N	-	-	N12
043	00:41:34.99	+41:05:52.3	N	-	-	N12
044	00:41:41.81	+40:37:11.5	N	-	-	N12
045	00:41:43.00	+41:18:59.7	N	-	-	N12
046	00:41:43.09	+40:40:45.9	N	-	-	N12
047	00:41:44.47	+40:45:17.1	N	-	-	N12
048	00:41:45.33	+41:21:04.0	N	-	-	N12
049	00:41:47.24	+41:06:47.5	N	-	-	N12
050	00:41:48.27	+41:17:39.9	N	-	-	N12
051	00:41:54.62	+40:47:13.8	N	-	-	N12
052	00:42:03.94	+41:25:54.5	N	-	-	N12
053	00:42:11.16	+40:56:48.0	N	-	-	N12
054	00:42:13.21	+40:50:51.8	N	-	-	N12
055	00:42:14.36	+41:25:42.3	N	-	-	N12
056	00:42:34.42	+41:30:24.2	N	-	-	N12
057	00:42:38.90	+41:00:02.0	N	-	-	N12
058	00:42:40.81	+41:02:41.6	N	-	-	N12
059	00:42:42.03	+41:23:14.9	Y	S	S	N12
060	00:42:42.33	+41:39:22.7	N	-	-	N12
061	00:42:47.12	+40:56:57.1	N	-	-	N12
062	00:42:49.84	+41:02:15.7	N	-	-	N12
063	00:42:54.65	+41:02:26.1	N	-	-	N12
064	00:42:56.05	+41:35:43.7	N	-	-	N12
065	00:42:56.85	+41:38:37.2	N	-	-	N12
066	00:42:57.62	+41:37:27.8	N	-	-	N12
067	00:43:02.05	+41:37:46.7	N	-	-	N12
068	00:43:02.76	+41:37:53.6	N	-	-	N12
069	00:43:04.34	+41:22:23.4	Y	S	S	N12
070	00:43:06.11	+41:38:13.7	N	-	-	N12
071	00:43:08.25	+41:37:36.3	N	-	-	N12
072	00:43:10.19	+41:37:44.0	N	-	-	N12
073	00:43:16.44	+41:45:12.4	N	-	-	N12
074	00:43:21.48	+41:41:55.5	N	-	-	N12
075	00:43:24.95	+41:18:03.2	Y	S	S	N12
076	00:43:25.68	+41:18:30.2	Y	S	S	N12
077	00:43:27.92	+41:42:07.3	N	-	-	N12
078	00:43:28.06	+41:42:12.3	N	-	-	N12
079	00:43:30.76	+41:27:34.7	Y	S	S	N12
080	00:43:31.17	+41:12:03.5	Y	M	S	N12
081	00:43:34.92	+41:09:53.2	Y	M	M	N12
082	00:43:36.51	+41:23:15.1	Y	S	S	N12
083	00:43:37.10	+41:42:37.1	N	-	-	N12
084	00:43:41.72	+41:23:04.2	Y	M	S	N12
085	00:43:44.48	+41:11:42.0	Y	M	S	N12
086	00:43:47.01	+41:12:38.0	Y	M	M	N12

Table A1. *Cont.*

(1) ID	(2) RA	(3) Dec	(4) F275W	(5) n(3.″3)	(6) n(1.″1)	(7) Ref
087	00:43:49.72	+41:12:43.4	Y	M	M	N12
088	00:43:53.34	+41:46:38.9	N	-	-	N12
089	00:43:57.31	+41:48:46.2	N	-	-	N12
090	00:44:03.39	+41:15:18.8	N	-	-	N12
091	00:44:06.39	+41:19:21.0	Y	S	S	N12
092	00:44:06.68	+41:16:12.0	Y	M	S	N12
093	00:44:08.58	+41:21:21.2	Y	S	S	N12
094	00:44:10.17	+41:32:53.1	Y	M	S	N12
095	00:44:10.91	+41:16:23.2	Y	S	S	N12
096	00:44:12.44	+41:29:41.7	Y	M	S	N12
097	00:44:13.06	+41:19:20.5	Y	M	S	N12
098	00:44:15.77	+41:19:52.5	Y	S	S	N12
099	00:44:16.20	+41:21:03.5	Y	M	M	N12
100	00:44:19.92	+41:17:51.2	Y	M	M	N12
101	00:44:20.58	+41:54:12.5	N	-	-	N12
102	00:44:22.24	+41:18:58.4	Y	M	S	N12
103	00:44:25.10	+41:20:50.0	Y	M	M	N12
104	00:44:25.43	+41:20:44.7	Y	M	M	N12
105	00:44:25.83	+41:50:19.4	N	-	-	N12
106	00:44:26.17	+41:22:10.8	Y	M	S	N12
107	00:44:26.32	+41:34:19.8	Y	S	S	N12
108	00:44:29.89	+41:20:21.6	Y	M	M	N12
109	00:44:30.04	+41:52:37.1	Y	M	M	N12
110	00:44:34.57	+41:24:24.4	Y	S	S	N12
111	00:44:35.15	+41:25:45.2	Y	M	S	N12
112	00:44:36.22	+41:22:57.3	Y	S	S	N12
113	00:44:36.52	+41:22:02.0	Y	S	S	N12
114	00:44:37.61	+41:52:03.3	Y	S	S	N12
115	00:44:43.10	+41:26:19.6	Y	M	M	N12
116	00:44:44.00	+41:27:39.9	Y	M	S	N12
117	00:44:44.87	+41:28:00.7	Y	M	S	N12
118	00:44:45.61	+41:28:06.5	Y	S	S	N12
119	00:44:45.90	+41:58:03.8	N	-	-	N12
120	00:44:49.41	+41:30:20.7	Y	S	S	N12
121	00:44:51.98	+41:29:11.6	Y	M	M	N12
122	00:44:53.06	+41:26:01.7	Y	S	S	N12
123	00:44:53.52	+41:53:54.3	Y	M	M	N12
124	00:44:55.63	+41:31:05.1	Y	M	M	N12
125	00:44:55.82	+41:29:19.2	Y	S	S	N12
126	00:45:00.96	+41:30:58.8	Y	M	M	N12
127	00:45:02.78	+41:55:33.7	Y	M	M	N12
128	00:45:06.50	+41:34:25.1	N	-	-	N12
129	00:45:09.18	+41:40:21.4	Y	M	S	N12
130	00:45:10.39	+41:36:46.6	Y	M	M	N12
131	00:45:11.21	+42:05:21.7	N	-	-	N12
132	00:45:11.27	+41:38:15.3	Y	M	S	N12
133	00:45:13.68	+41:37:42.5	Y	M	M	N12
134	00:45:14.10	+41:37:35.2	Y	S	S	N12
135	00:45:17.56	+41:39:22.0	Y	M	M	N12
136	00:45:17.89	+41:52:09.5	Y	M	S	N12
137	00:45:20.80	+41:51:00.0	Y	S	S	N12
138	00:45:22.78	+42:03:18.2	Y	S	S	N12
139	00:45:24.26	+41:53:52.5	Y	S	S	N12

Table A1. *Cont.*

(1) ID	(2) RA	(3) Dec	(4) F275W	(5) n(3.″3)	(6) n(1.″1)	(7) Ref
140	00:45:30.61	+41:46:39.2	Y	S	S	N12
141	00:45:31.16	+42:06:58.1	N	-	-	N12
142	00:45:37.05	+41:43:02.4	Y	M	S	N12
143	00:45:37.10	+41:42:01.4	Y	M	M	N12
144	00:45:37.28	+41:43:05.2	Y	M	S	N12
145	00:45:39.15	+41:47:54.0	Y	M	S	N12
146	00:45:39.35	+41:44:39.8	Y	M	S	N12
147	00:45:41.29	+41:55:04.0	Y	M	S	N12
148	00:45:42.26	+41:45:10.1	Y	M	S	N12
149	00:45:44.65	+41:52:41.0	Y	M	S	N12
150	00:45:51.12	+42:10:15.4	N	-	-	N12
151	00:45:51.35	+41:42:42.0	N	-	-	N12
152	00:46:28.51	+42:11:27.6	Y	S	S	N12
153	00:46:45.02	+42:13:01.3	Y	S	S	N12
154	00:46:55.89	+42:00:15.1	Y	M	M	N12
155	00:40:19.66	+40:42:32.5	N	-	-	N23
156	00:40:31.21	+40:41:28.1	N	-	-	N23
157	00:40:32.57	+40:39:01.3	N	-	-	N23
158	00:40:39.59	+40:44:49.5	N	-	-	N23
159	00:40:42.44	+40:45:05.3	N	-	-	N23
160	00:40:54.05	+40:37:08.3	N	-	-	N23
161	00:43:26.06	+41:42:60.0	N	-	-	N23
162	00:43:38.95	+41:43:27.0	N	-	-	N23
163	00:43:41.15	+41:44:13.6	N	-	-	N23
164	00:43:53.03	+41:21:41.0	Y	S	S	N23
165	00:43:59.44	+41:48:23.9	N	-	-	N23
166	00:44:06.41	+41:20:20.8	Y	S	S	N23
167	00:44:08.13	+41:21:00.6	Y	M	S	N23
168	00:44:13.56	+41:20:04.7	Y	M	M	N23
169	00:44:18.10	+41:18:50.8	Y	M	M	N23
170	00:44:25.09	+41:20:46.4	Y	M	M	N23
171	00:44:31.39	+41:21:14.0	Y	M	S	N23
172	00:44:33.91	+41:25:01.2	Y	M	S	N23
173	00:44:38.04	+41:25:18.7	Y	M	S	N23
174	00:43:43.61	+41:45:27.9	N	-	-	S16

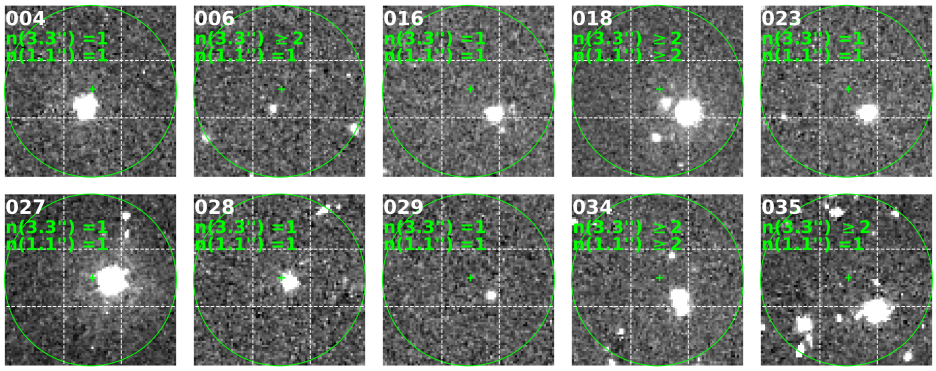

Figure A1. *Cont.*

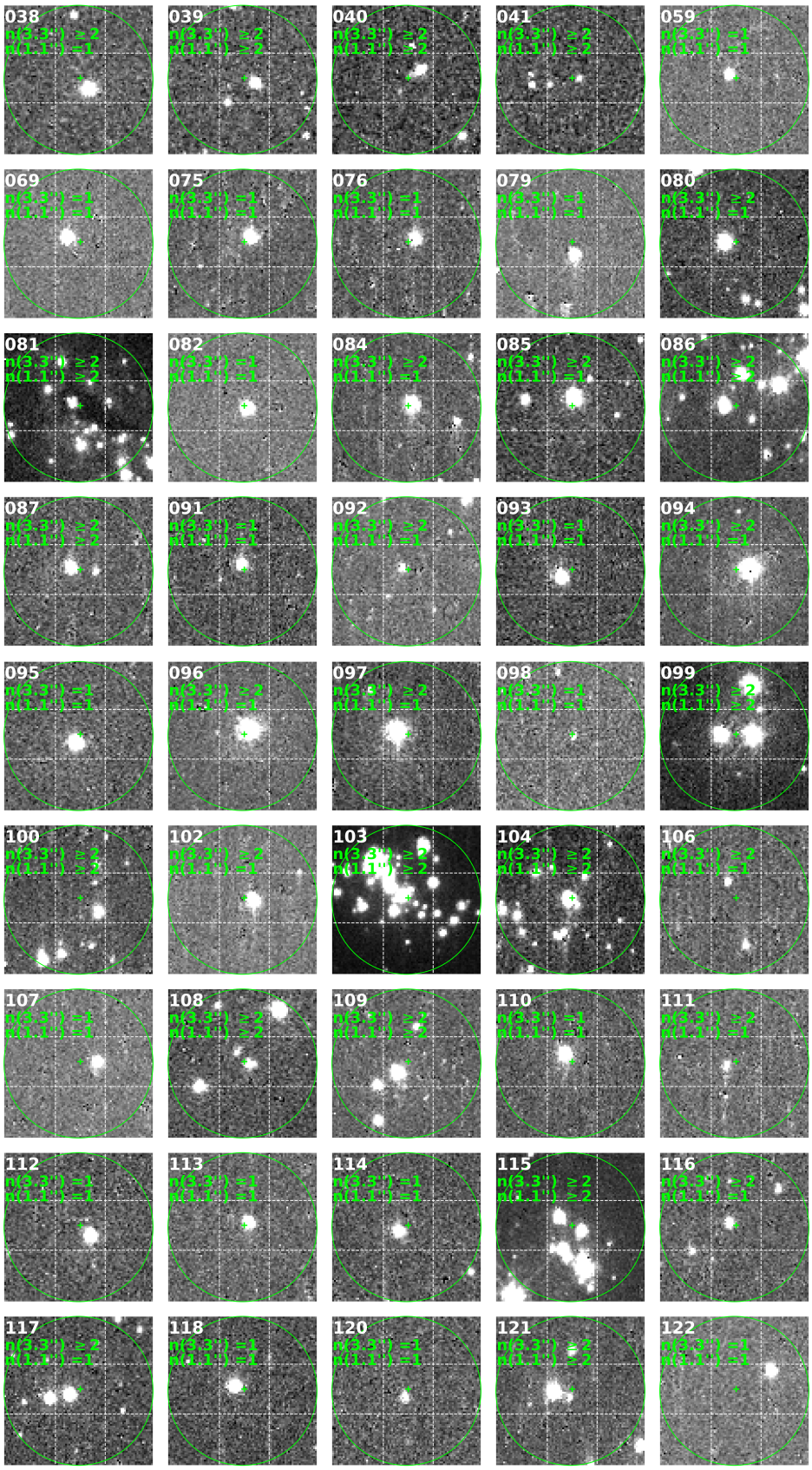

Figure A1. *Cont.*

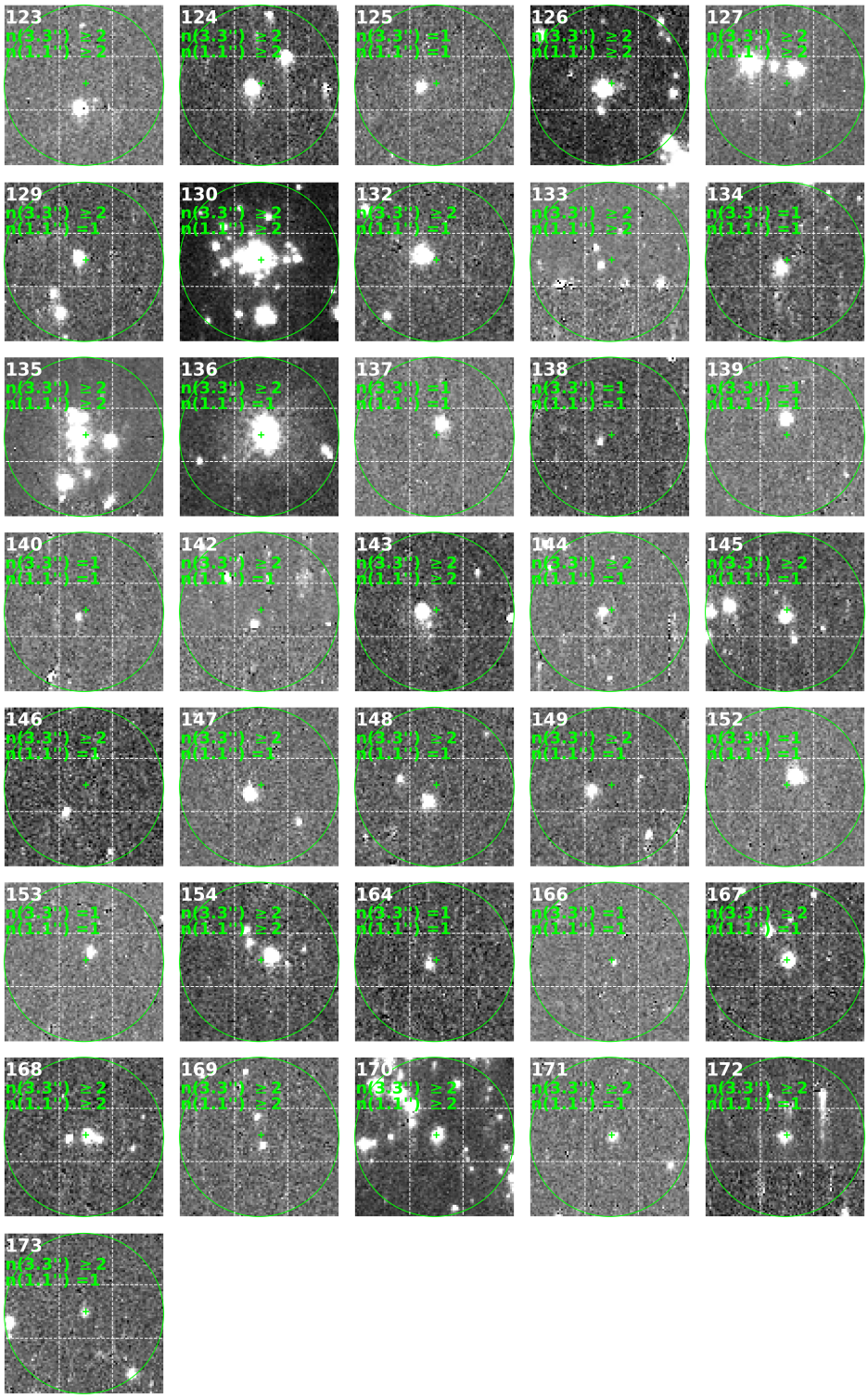

Figure A1. HST F275W images for matched targets. In each panel, ID is shown in the upper left. The green circle, with a diameter of 3.″3, represents the position of the LAMOST fiber. The green cross marks the target center coordinates, of which (RA, Dec) are listed in the Table A1. The white dashed lines divide the image into 3 × 3 grids, with each grid covering 1.″1. N(3.″3) and n(1.″1) denote the number of bright sources in the FOV of 3.″3 and 1.″1, respectively.

References

1. Meynet, G.; Maeder, A. Stellar evolution with rotation. XI. Wolf-Rayet star populations at different metallicities. *Astron. Astrophys.* **2005**, *429*, 581–598. [CrossRef]
2. van Loon, J.T.; Cioni, M.R.L.; Zijlstra, A.A.; Loup, C. An empirical formula for the mass-loss rates of dust-enshrouded red supergiants and oxygen-rich Asymptotic Giant Branch stars. *Astron. Astrophys.* **2005**, *438*, 273–289. [CrossRef]
3. Chieffi, A.; Limongi, M. The Presupernova Core Mass-Radius Relation of Massive Stars: Understanding Its Formation and Evolution. *Astrophys. J.* **2020**, *890*, 43. [CrossRef]
4. Ekström, S.; Georgy, C.; Eggenberger, P.; Meynet, G.; Mowlavi, N.; Wyttenbach, A.; Granada, A.; Decressin, T.; Hirschi, R.; Frischknecht, U.; et al. Grids of stellar models with rotation. I. Models from 0.8 to 120 $M_{\odot}$ at solar metallicity (Z = 0.014). *Astron. Astrophys.* **2012**, *537*, A146. [CrossRef]
5. Paxton, B.; Bildsten, L.; Dotter, A.; Herwig, F.; Lesaffre, P.; Timmes, F. Modules for Experiments in Stellar Astrophysics (MESA). *Astrophys. J. Suppl.* **2011**, *192*, 3. [CrossRef]
6. Bressan, A.; Marigo, P.; Girardi, L.; Salasnich, B.; Dal Cero, C.; Rubele, S.; Nanni, A. PARSEC: Stellar tracks and isochrones with the PAdova and TRieste Stellar Evolution Code. *Mon. Not. R. Astron. Soc.* **2012**, *427*, 127–145. [CrossRef]
7. Eldridge, J.J.; Izzard, R.G.; Tout, C.A. The effect of massive binaries on stellar populations and supernova progenitors. *Mon. Not. R. Astron. Soc.* **2008**, *384*, 1109–1118. [CrossRef]
8. Eldridge, J.J.; Stanway, E.R. BPASS predictions for binary black hole mergers. *Mon. Not. R. Astron. Soc.* **2016**, *462*, 3302–3313. [CrossRef]
9. Crowther, P.A. Physical Properties of Wolf-Rayet Stars. *Annu. Rev. Astron. Astrophys.* **2007**, *45*, 177–219. [CrossRef]
10. Crowther, P.A.; Smith, L.J.; Willis, A.J. Fundamental parameters of Wolf-Rayet stars. V. The nature of the WN/C star WR 8. *Astron. Astrophys.* **1995**, *304*, 269.
11. Zhang, W.; Todt, H.; Wu, H.; Shi, J.; Hsia, C.H.; Wu, Y.; Wu, C.; Zhao, Y.; Zhang, T.; Hou, Y. A New Transition Wolf-Rayet WN/C Star in the Milky Way. *Astrophys. J.* **2020**, *902*, 62. [CrossRef]
12. Sander, A.A.C.; Lefever, R.R.; Josiek, J.; Higgins, E.R.; Hirschi, R.; Oskinova, L.M.; Pauli, D.; Pritzkuleit, M.; Gallagher, J.S.; Hamann, W.R.; et al. Discovery of a transitional type of evolved massive star with a hard ionizing flux. *Nat. Astron.* **2025**, *10*, 290–305 . [CrossRef]
13. Callingham, J.R.; Tuthill, P.G.; Pope, B.J.S.a. Anisotropic winds in a Wolf-Rayet binary identify a potential gamma-ray burst progenitor. *Nat. Astron.* **2019**, *3*, 82–87. [CrossRef]
14. Allen, D.A.; Wright, A.E.; Goss, W.M. The dwarf emission galaxy He 2-10. *Mon. Not. R. Astron. Soc.* **1976**, *177*, 91. [CrossRef]
15. Osterbrock, D.E.; Cohen, R.D. Two galaxies with Wolf-rayet features in their spectra. *Astrophys. J.* **1982**, *261*, 64–69. [CrossRef] [PubMed]
16. Zhang, W.; Kong, X.; Li, C.; Zhou, H.Y.; Cheng, F.Z. Wolf-Rayet Galaxies in the Sloan Digital Sky Survey: The Metallicity Dependence of the Initial Mass Function. *Astrophys. J.* **2007**, *655*, 851–862. [CrossRef] [PubMed]
17. Brinchmann, J.; Kunth, D.; Durret, F. Galaxies with Wolf-Rayet signatures in the low-redshift Universe. A survey using the Sloan Digital Sky Survey. *Astron. Astrophys.* **2008**, *485*, 657–677. [CrossRef]
18. Agienko, K.B.; Guseva, N.G.; Izotov, Y.I. Sample of Wolf-Rayet galaxies from the SLOAN digital sky survey. *Kinemat. Phys. Celest. Bodies* **2013**, *29*, 131–140. [CrossRef]
19. Liang, F.H.; Li, C.; Li, N.; Yan, R.; Mo, H.; Zhang, W.; Machuca, C.; Roman-Lopes, A. Wolf-Rayet Galaxies in SDSS-IV MaNGA. I. Catalog Construction and Sample Properties. *Astrophys. J.* **2020**, *896*, 121. [CrossRef]
20. Liang, F.H.; Li, C.; Li, N.; Zhou, S.; Yan, R.; Mo, H.; Zhang, W. Wolf-Rayet Galaxies in SDSS-IV MaNGA. II. Metallicity Dependence of the High-mass Slope of the Stellar Initial Mass Function. *Astrophys. J.* **2021**, *923*, 120. [CrossRef]
21. Moffat, A.F.J.; Shara, M.M. Wolf-Rayet stars in the Local Group galaxies M 31 and NGC 6822. *Astrophys. J.* **1983**, *273*, 544–561. [CrossRef]
22. Massey, P.; Armandroff, T.E.; Conti, P.S. Massive stars in M31. *Astron. J.* **1986**, *92*, 1303–1333. [CrossRef] [PubMed]
23. Neugent, K.F.; Massey, P.; Georgy, C. The Wolf-Rayet Content of M31. *Astrophys. J.* **2012**, *759*, 11. [CrossRef]
24. Shara, M.M.; Mikołajewska, J.; Caldwell, N.; Iłkiewicz, K.; Drozd, K.; Zurek, D. The first transition Wolf-Rayet WN/C star in M31. *Mon. Not. R. Astron. Soc.* **2016**, *455*, 3453–3457. [CrossRef]
25. Neugent, K.F.; Massey, P. Newly Discovered Wolf-Rayet Stars in M31. *Astron. J.* **2023**, *166*, 68. [CrossRef]
26. Massey, P.; Neugent, K.F.; Dorn-Wallenstein, T.Z.; Eldridge, J.J.; Stanway, E.R.; Levesque, E.M. Testing Evolutionary Models with Red Supergiant and Wolf-Rayet Populations. *Astrophys. J.* **2021**, *922*, 177. [CrossRef]
27. Vink, J.S.; de Koter, A. On the metallicity dependence of Wolf-Rayet winds. *Astron. Astrophys.* **2005**, *442*, 587–596. [CrossRef]
28. Eldridge, J.J.; Vink, J.S. Implications of the metallicity dependence of Wolf-Rayet winds. *Astron. Astrophys.* **2006**, *452*, 295–301. [CrossRef]
29. Neugent, K.; Massey, P. The Wolf–Rayet Content of the Galaxies of the Local Group and Beyond. *Galaxies* **2019**, *7*, 74. [CrossRef]

30. Woosley, S.E.; Heger, A. Nucleosynthesis and remnants in massive stars of solar metallicity. *Phys. Rep.* **2007**, *442*, 269–283. [CrossRef]
31. Limongi, M.; Chieffi, A. Presupernova Evolution and Explosive Nucleosynthesis of Rotating Massive Stars in the Metallicity Range $-3 \leq$ [Fe/H] ≤ 0. *Astrophys. J. Suppl.* **2018**, *237*, 13. [CrossRef]
32. Neugent, K.F.; Massey, P. The Wolf-Rayet Content of M33. *Astrophys. J.* **2011**, *733*, 123. [CrossRef]
33. Conti, P.S.; Massey, P. Spectroscopic Studies of Wolf-Rayet Stars. IV. Optical Spectrophotometry of the Emission Lines in Galactic and Large Magellanic Cloud Stars. *Astrophys. J.* **1989**, *337*, 251. [CrossRef] [PubMed]
34. Ryon, J.E.; Bastian, N.; Adamo, A.; Konstantopoulos, I.S.; Gallagher, J.S.; Larsen, S.; Hollyhead, K.; Silva-Villa, E.; Smith, L.J. Sizes and shapes of young star cluster light profiles in M83. *Mon. Not. R. Astron. Soc.* **2015**, *452*, 525–539. [CrossRef]
35. Brown, G.; Gnedin, O.Y. Radii of young star clusters in nearby galaxies. *Mon. Not. R. Astron. Soc.* **2021**, *508*, 5935–5953. [CrossRef]
36. Wang, S.G.; Su, D.Q.; Chu, Y.Q.; Cui, X.; Wang, Y.N. Special configuration of a very large Schmidt telescope for extensive astronomical spectroscopic observation. *Appl. Opt.* **1996**, *35*, 5155–5161. [CrossRef] [PubMed]
37. Su, D.Q.; Cui, X.Q. Active Optics in LAMOST. *Chin. J. Astron. Astrophys.* **2004**, *4*, 1. [CrossRef]
38. Cui, X.Q.; Zhao, Y.H.; Chu, Y.Q.; Li, G.P.; Li, Q.; Zhang, L.P.; Su, H.J.; Yao, Z.Q.; Wang, Y.-N.; Xing, X.-Z. The Large Sky Area Multi-Object Fiber Spectroscopic Telescope (LAMOST). *Res. Astron. Astrophys.* **2012**, *12*, 1197–1242. [CrossRef]
39. Zhao, G.; Zhao, Y.H.; Chu, Y.Q.; Jing, Y.P.; Deng, L.C. LAMOST spectral survey—An overview. *Res. Astron. Astrophys.* **2012**, *12*, 723–734. [CrossRef]
40. Luo, A.L.; Zhao, Y.H.; Zhao, G.; Deng, L.C.; Liu, X.W.; Jing, Y.P.; Wang, G.; Zhang, H.T.; Shi, J.R.; Cui, X.Q. The first data release (DR1) of the LAMOST regular survey. *Res. Astron. Astrophys.* **2015**, *15*, 1095. [CrossRef]
41. Humphreys, R.M.; Pennington, R.L.; Jones, T.J.; Ghigo, F.D. The Red Supergiants in M31: Spectra, Colors, and Luminosities. *Astron. J.* **1988**, *96*, 1884. [CrossRef] [PubMed]
42. Johnson, L.C.; Seth, A.C.; Dalcanton, J.J.; Wallace, M.L.; Simpson, R.J.; Lintott, C.J.; Kapadia, A.; Skillman, E.D.; Caldwell, N.; Fouesneau, M.; et al. PHAT Stellar Cluster Survey. II. Andromeda Project Cluster Catalog. *Astrophys. J.* **2015**, *802*, 127. [CrossRef]
43. Dalcanton, J.J.; Williams, B.F.; Lang, D.; Lauer, T.R.; Kalirai, J.S.; Seth, A.C.; Dolphin, A.; Rosenfield, P.; Weisz, D.R.; Bell, E.F.; et al. The Panchromatic Hubble Andromeda Treasury. *Astrophys. J. Suppl.* **2012**, *200*, 18. [CrossRef]
44. Charlot, S.; Fall, S.M. A Simple Model for the Absorption of Starlight by Dust in Galaxies. *Astrophys. J.* **2000**, *539*, 718–731. [CrossRef]
45. Li, N.; Li, C.; Mo, H.; Zhou, S.; Liang, F.h.; Boquien, M.; Drory, N.; Fernández-Trincado, J.G.; Greener, M.; Riffel, R. Estimating Dust Attenuation From Galactic Spectra. II. Stellar and Gas Attenuation in Star-forming and Diffuse Ionized Gas Regions in MaNGA. *Astrophys. J.* **2021**, *917*, 72. [CrossRef]
46. Proxauf, B.; Öttl, S.; Kimeswenger, S. Upgrading electron temperature and electron density diagnostic diagrams of forbidden line emission. *Astron. Astrophys.* **2014**, *561*, A10. [CrossRef]
47. Pettini, M.; Pagel, B.E.J. [OIII]/[NII] as an abundance indicator at high redshift. *Mon. Not. R. Astron. Soc.* **2004**, *348*, L59–L63. [CrossRef]
48. Dopita, M.A.; Kewley, L.J.; Sutherland, R.S.; Nicholls, D.C. Chemical abundances in high-redshift galaxies: A powerful new emission line diagnostic. *Astrophys. Space Sci.* **2016**, *361*, 61. [CrossRef]
49. Asplund, M.; Grevesse, N.; Sauval, A.J.; Scott, P. The Chemical Composition of the Sun. *Annu. Rev. Astron. Astrophys.* **2009**, *47*, 481–522. [CrossRef]
50. Gräfener, G.; Koesterke, L.; Hamann, W.R. Line-blanketed model atmospheres for WR stars. *Astron. Astrophys.* **2002**, *387*, 244–257. [CrossRef]
51. Hamann, W.R.; Gräfener, G. A temperature correction method for expanding atmospheres. *Astron. Astrophys.* **2003**, *410*, 993–1000. [CrossRef]
52. Sander, A.; Shenar, T.; Hainich, R.; Gímenez-García, A.; Todt, H.; Hamann, W.R. On the consistent treatment of the quasi-hydrostatic layers in hot star atmospheres. *Astron. Astrophys.* **2015**, *577*, A13. [CrossRef]
53. Hamann, W.R.; Gräfener, G. Grids of model spectra for WN stars, ready for use. *Astron. Astrophys.* **2004**, *427*, 697–704. [CrossRef]
54. Todt, H.; Sander, A.; Hainich, R.; Hamann, W.R.; Quade, M.; Shenar, T. Potsdam Wolf-Rayet model atmosphere grids for WN stars. *Astron. Astrophys.* **2015**, *579*, A75. [CrossRef]
55. Sander, A.; Hamann, W.R.; Todt, H. The Galactic WC stars. Stellar parameters from spectral analyses indicate a new evolutionary sequence. *Astron. Astrophys.* **2012**, *540*, A144. [CrossRef]
56. Hainich, R.; Ramachandran, V.; Shenar, T.; Sander, A.A.C.; Todt, H.; Gruner, D.; Oskinova, L.M.; Hamann, W.R. PoWR grids of non-LTE model atmospheres for OB-type stars of various metallicities. *Astron. Astrophys.* **2019**, *621*, A85. [CrossRef]
57. Dai, M.; Wang, S.; Jiang, B.; Li, Y. The Samples and Binary Fractions of Red Supergiants in M31 and M33 by the HST Observations. *Astrophys. J.* **2025**, *988*, 60. [CrossRef]
58. Bayo, A.; Rodrigo, C.; Barrado Y Navascués, D.; Solano, E.; Gutiérrez, R.; Morales-Calderón, M.; Allard, F. VOSA: Virtual observatory SED analyzer. An application to the Collinder 69 open cluster. *Astron. Astrophys.* **2008**, *492*, 277–287. [CrossRef]

59. Castelli, F.; Kurucz, R.L. New Grids of ATLAS9 Model Atmospheres. In *Proceedings of the Modelling of Stellar Atmospheres*; Piskunov, N., Weiss, W.W., Gray, D.F., Eds.; IAU Symposium; Astronomical Society of the Pacific (ASP): San Francisco, CA, USA, 2003; Volume 210, p. A20. [CrossRef]
60. Drout, M.R.; Massey, P.; Meynet, G.; Tokarz, S.; Caldwell, N. Yellow Supergiants in the Andromeda Galaxy (M31). *Astrophys. J.* **2009**, *703*, 441–460. [CrossRef]
61. Gordon, M.S.; Humphreys, R.M.; Jones, T.J. Luminous and Variable Stars in M31 and M33. III. The Yellow and Red Supergiants and Post-red Supergiant Evolution. *Astrophys. J.* **2016**, *825*, 50. [CrossRef]
62. Wu, H.; Huang, Y.; Zhang, H.; Yuan, H.; Huo, Z.; Liu, C. The LAMOST Spectroscopic Survey of Supergiants in M31 and M33. *Res. Astron. Astrophys.* **2025**, *25*, 015012. [CrossRef]
63. Smercina, A.; Fetherolf, T.; Koch, E.W.; Martocchia, S.; Mihos, C.; Williams, B.F. Resolving Individual Stars in Nearby Large Galaxies with the Habitable Worlds Observatory. *arXiv* **2025**, arXiv:2507.01960. [CrossRef]

Disclaimer/Publisher's Note: The statements, opinions and data contained in all publications are solely those of the individual author(s) and contributor(s) and not of MDPI and/or the editor(s). MDPI and/or the editor(s) disclaim responsibility for any injury to people or property resulting from any ideas, methods, instructions or products referred to in the content.